Modelling nanostructures with vicinal surfaces

2006 J. Phys.: Condens. Matter 18 S27

(http://iopscience.iop.org/0953-8984/18/13/S03)

INSTITUTE OF PHYSICS PUBLISHING JOURNAL OF PHYSICS: CONDENSED MATTER

J. Phys.: Condens. Matter **18** (2006) S27–S49 doi:10.1088/0953-8984/18/13/S03

Modelling nanostructures with vicinal surfaces

A Mugarza[1,4], F Schiller[1,2], J Kuntze[3], J Cordón[1], M Ruiz-Osés[1] and J E Ortega[1,2]

[1] Departamento de Física Aplicada I and Centro Mixto CSIC/UPV, Universidad del País Vasco, Plaza de Oñate 2, E-20018 Donostia-San Sebastián, Spain
[2] Donostia International Physics Center, Paseo Manuel Lardizabal 4, E-20018 Donostia-San Sebastián, Spain
[3] Institut für Experimentelle und Angewandte Physik, Olshausenstraße 40, D-24098 Kiel, Germany

Received 9 November 2005
Published 13 March 2006
Online at stacks.iop.org/JPhysCM/18/S27

Abstract

Vicinal surfaces of the (111) plane of noble metals are characterized by free-electron-like surface states that scatter at one-dimensional step edges, making them ideal model systems to test the electronic properties of periodic lateral nanostructures. Here we use high-resolution, angle-resolved photoemission to analyse the evolution of the surface state on a variety of vicinal surface structures where both the step potential barrier and the superlattice periodicity can vary. A transition in the electron dimensionality is found as we vary the terrace size in single-phase step arrays. In double-phase, periodic faceted surfaces, we observe surface states that characterize each of the phases.

(Some figures in this article are in colour only in the electronic version)

1. Introduction

Vicinal surfaces can be ideal templates to grow self-assembled arrays of nanostructures [1–6]. Their step lattice patterns a one-dimensional mesh, inducing the growth of stripes, wires and dots with a long-range, single-domain order. For this purpose, it is crucial to control both the stability of well ordered step lattices and further growth of nanostructures. A careful analysis of the role of the surface electronic structure on these processes is also necessary. Indeed, certain vicinal structures can be stabilized by the electronic step–step interaction [7, 8], or by minimizing the electronic energy by opening a band-gap at the Fermi level [9]. On the other hand, surface state mediated adsorbate interactions can play an important role in the growth of clusters [10, 11] and induce self-assembly in some cases [12].

[4] Present address: Lawrence Berkeley National Laboratory, University of California, 1 Cyclotron Road, Berkeley, CA 94720, USA.

Vicinal surfaces can also be considered themselves as simple one-dimensional (1D) nanostructures. In particular, noble metal surfaces vicinal to the (111) plane contain a surface state which propagates along the surface, interacting strongly with the step lattice. The interesting point is that superlattice parameters such as the step periodicity and the stripe width in faceted surfaces can be tuned in order to carefully study the transition from arrays of non-interacting nano-objects (terraces), where electron states are confined, to lateral coupling between terraces, which leads to superlattice states. This property makes them ideal model systems to study the electronic properties of ordered nanostructures.

In this review we report a study of surface states in Cu(111) and Au(111) vicinal surfaces representing a complete set of structures. The most simple step structures are single-phase vicinals, i.e., 1D arrays of steps with a single step-lattice constant d. Such surfaces have been studied by a number of groups in the past. Both surface and image states have been measured with photoemission techniques such as angle-resolved photoemission spectroscopy (ARPES) [9, 13–27], angle-resolved two-photon photoemission spectroscopy (AR2PPE) [28–33] or scanning tunnelling microscopy (STM) [14, 34, 35]. The most remarkable observation is the changing dimensionality of the surface state as one varies d. The results obtained in our study are compared to those reported by other groups. We discuss the different physical phenomena that can explain the transition from 1D to 2D surface states around a critical d value, such as surface and bulk state mixing, surface state depopulation, lattice disorder and band-gap opening at the Fermi level. We pay special attention to the role of parameters that prevent a proper determination of surface state dimensionality and critical terrace size, such as finite size distribution and experimental resolution. This is also necessary to draw conclusions for future studies of more complex nanostructures. Finally, double-phase vicinals are studied, where two phases with different step lattice constants form a periodic stripe array. These surfaces exhibit more complex electronic structures with distinct surface states that characterize each of the phases. We also observe two different regimes, where surface states propagate or get confined within surface phases, leading to phase-size effects.

2. Experimental details

In this study we use vicinal surfaces that have already been characterized by STM by other groups. Vicinal Cu and Au surfaces [v-Cu(111), v-Au(111)] were analysed by the group of S Speller at the University of Osnabrück [36] and by the group of S Rousset at the University of Paris VI [37], respectively. The terrace width distributions (TWDs) obtained in their analyses were used in this work.

The electronic structure was analysed by ARPES, at various sites and under different experimental conditions. Au(223) was measured at the SU8 beam line in the synchrotron LURE in Paris, using a VWS electron analyser with energy and angular resolution of 50 meV and 1° respectively, and at 300 K. Au(23 23 21), Au(9 9 11), Cu(335) and Ag/Cu(335) were measured at the PGM beam line in the Synchrotron Radiation Center of the University of Wisconsin-Madison, using a Scienta SES200 analyser with energy and angular resolution of 30 meV and 0.4° respectively, and at 120 K. The experiments with Au(887) were performed at $T = 150$ K at the University of Technology Dresden using a Gammadata VUV 5000 high-intensity He discharge lamp and a Scienta SES200 analyser with energy and angular resolutions of 30 meV and 0.3°, respectively.

All the surfaces were prepared *in situ* in ultra-high vacuum (UHV) by repeated cycles of sputtering with Ar^+ ions at 1 kV and further annealing to 800 K. The quality of the surface and the step lattice were checked *in situ* by analysing the spot profile and their splitting in low-energy electron diffraction (LEED) patterns.

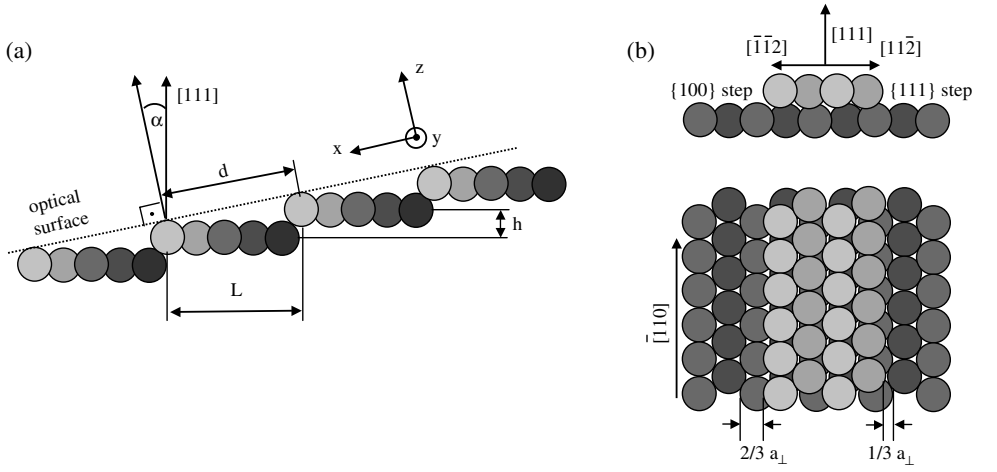

Figure 1. (a) Schematic side view of a single vicinal surface indicating the relevant parameters. (b) Top and side views of (111) planes showing {100} and {111} step types.

3. Single-phase vicinal surfaces

Vicinal surfaces are characterized by a small miscut angle with respect to a high symmetry plane. If the azimuthal orientation is chosen to be another high symmetry direction, the clean vicinal surface usually displays flat terraces of the high symmetry plane separated by straight steps. Due to the repulsive step–step interaction [38, 39] the steps generally appear regularly spaced with a single periodicity that can be continuously varied. Thus, we shall call them single-phase vicinals. The high symmetry plane is the (111) and the azimuthal orientation is the $[\bar{1}10]$, which can lead to two different step types, {100} and {111}, as shown in the schematic description of figure 1(b). The resulting Miller indices are $(m, m, m + 2)$ and $(m + 1, m + 1, m - 1)$ for {100} and {111} step type, respectively, where $m + 2/3$ and $m + 1/3$ are the numbers of atomic rows on each terrace. For the small miscut angles studied in this work, the step periodicity d and the terrace size L are very similar, so d will be used to refer to both of them throughout the text.

In table 1 we summarize the structural properties of the different surfaces studied in this work, as well as others measured elsewhere [15, 16, 21–25, 27, 40]. Two representative STM images are displayed in figure 2. As can be read in table 1, the normalized TWD $\bar{\sigma} = \Delta d/d$ is larger for v-Cu(111) than for v-Au(111). This is mainly due to particularly stable terrace sizes found in certain v-Au(111) due to the interaction between the surface herringbone reconstruction and the step lattice [37]. In the case of v-Cu(111) a narrower TWD has been observed for surfaces with {100} step type compare to the ones with {111} step type, due to a weaker step–step interaction in the latter [36]. Altogether, the terrace sizes studied range from 7 to 56 Å.

The interaction between the surface electron and the step array can be treated within the framework of a 1D Kronig–Penney (KP) model [41, 42], which consists basically of an infinite array of 1D potential barriers. It has been shown that for any shape of the potential barrier one can always replace it by a suitably chosen δ-function $V(x) = \Sigma_n U_0 b\delta(x - nd)$ [43] (for a square barrier, U_0 corresponds to the height and b to the width of the barrier). In this case the energy dispersion can be expressed as

$$E(k_x) = E_0 + \frac{\hbar^2}{2m^*}\frac{1}{d^2}[\cos^{-1}(|T|\cos k_x d) - \phi]^2 \qquad (1)$$

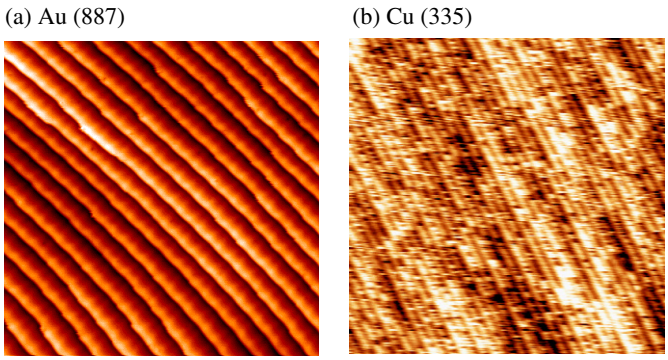

Figure 2. STM images of two single-phase vicinal (111) surfaces showing straight, regularly spaced steps. (a) Au(887), with terrace size $d = 39$ Å. Image size: 80×80 nm^2. (b) Cu(335), with terrace size $d = 8$ Å. Image size: 30×30 nm^2.

Table 1. Structural parameter list for the single-phase vicinal Cu(111) and Au(111) surfaces studied in this work (in bold), as well as others studied in the indicated references. The terrace size and miscut angle correspond to their nominal values. m stands for the number of atom rows per terrace. The normalized terrace width distribution $\tilde{\sigma}$ has been obtained from STM image analysis.

Vicinal index	Step-type	m	d (Å)	α (deg)	$\tilde{\sigma}$
Cu(10 10 11) [27]	{100}	20	45.9	2.6	0.25
Cu(778) [40]	{100}	14	32.6	3.7	—
Cu(556) [15, 16, 25]	{100}	10	23.7	5.1	—
Cu(779) [16]	{100}	7	16.9	7.0	—
Cu(557) [15, 16, 25]	{100}	5	12.6	9.4	0.185
Cu(223) [23, 24]	{100}	4	10.3	11.4	—
Cu(335) [27]	{100}	3	8.1	14.3	—
Cu(443) [16]	{111}	7	16.3	7.3	—
Cu(332) [16]	{111}	5	11.8	10.0	0.26
Au(223) [21, 25]	{100}	4	11.6	11.4	0.15
Au(23 23 21) [22, 25, 27]	{111}	22	56.4	2.4	0.11
Au(887) [17, 21, 25, 27]	{111}	15	39.0	3.4	0.10

where E_0 is the energy at the band bottom when $d \to \infty$, i.e., for a flat surface. $|T|$ and ϕ denote the modulus and the phase of the complex transmission coefficient. Both are energy dependent and can be expressed as

$$|T|^2 = \frac{1}{1 + (q_0/q)^2} \tag{2}$$

and

$$\phi = -\tan^{-1}(q_0/q) \tag{3}$$

where $q_0 = (m^*/\hbar^2) \cdot U_0 b$ and $q = \sqrt{(2m^*/\hbar^2)(E - E_0)}$. The effect of the potential barrier on the dispersion of the band can be visualized in figure 3(a). For a finite $U_0 b$ the free-electron-like parabola (solid line) splits into superlattice bands (dotted lines) separated by gaps and folded by superlattice wavevector $2\pi/d$ (vertical dotted lines). In addition, the band bottom is shifted in energy with respect to the free parabola. As we increase the potential barrier the band bottom shifts to higher energy and the bands become narrower, separated by a larger gap.

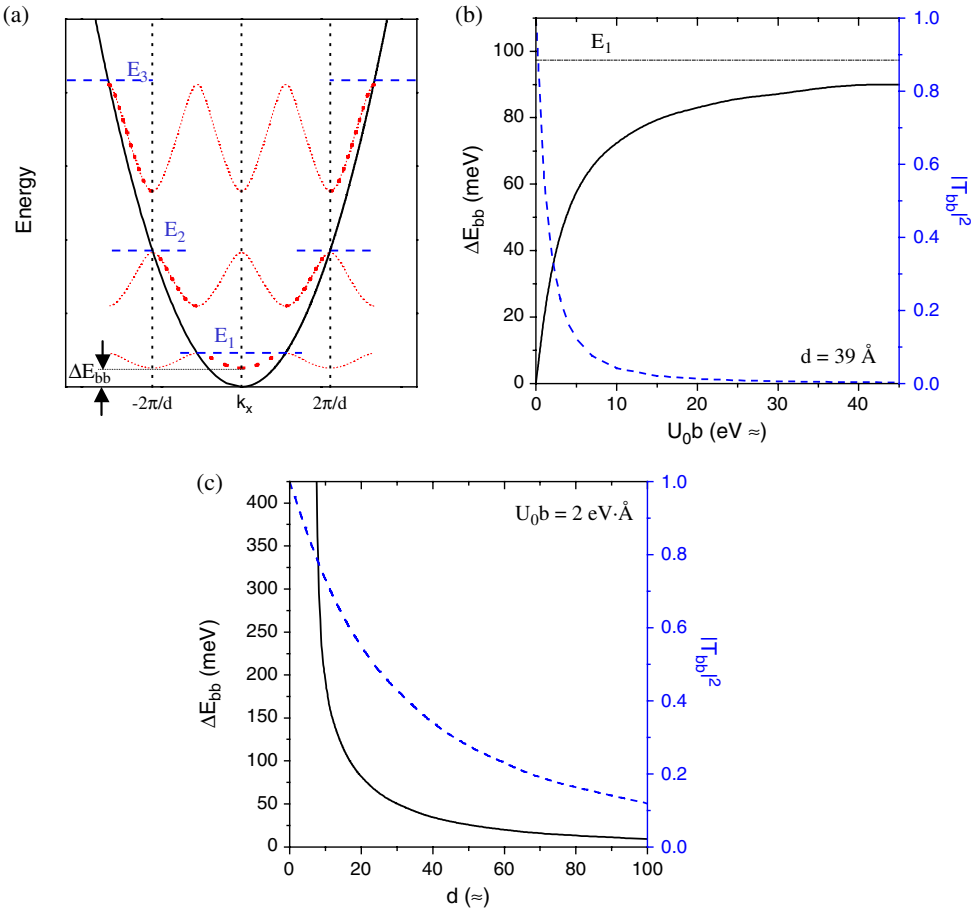

Figure 3. (a) Kronig–Penney bands for different potential barriers: $U_0b = 0$ (solid line), U_0b finite (dotted lines) and U_0b infinite (dashed lines). (b) Energy shift (solid line) and transmission probability (dashed line) at the band bottom as a function of potential barrier for $d = 39$ Å. (c) Energy shift (solid line) and transmission probability (dashed line) at the band bottom as a function of superlattice periodicity d, for $U_0b = 2$ eV Å.

For the limiting case of infinite barriers the superlattice bands transform into non-dispersing quantum well (QW) levels, with their intensity distribution along k_x centred at the crossing points with the free-electron parabola except for the $N = 1$ level, which is centred at $k_x = 0$ (dashed line). In figure 3(b) the energy shift $\Delta E_{\rm bb} = E_{\rm bb} - E_{\rm bb}^{U_0b=0}$ and the transmission probability $|T_{\rm bb}|$ of the band bottom are represented for $d = 39$ Å as a function of the potential barrier. Both $\Delta E_{\rm bb}$ and $|T_{\rm bb}|$ vary rapidly with U_0b within the first few eV Å, asymptotically reaching $\Delta E_{\rm bb} = E_1$, the energy of the first QW level, and $|T_{\rm bb}| = 0$ as $U_0b \longrightarrow \infty$. It is interesting to note that even for a fixed barrier, increasing the superlattice periodicity results in a downwards energy shift of the whole band, and thus a decrease of $|T_{\rm bb}|$, as shown in figure 3(c) for $U_0b = 2$ eV Å. Therefore, both the potential barrier and the superlattice periodicity have to be taken into account in order to study the electron coupling through the steps.

The results obtained with the set of single-phase vicinal surfaces can be summarized with the three representative cases shown in figure 4. The peaks at each energy distribution curve

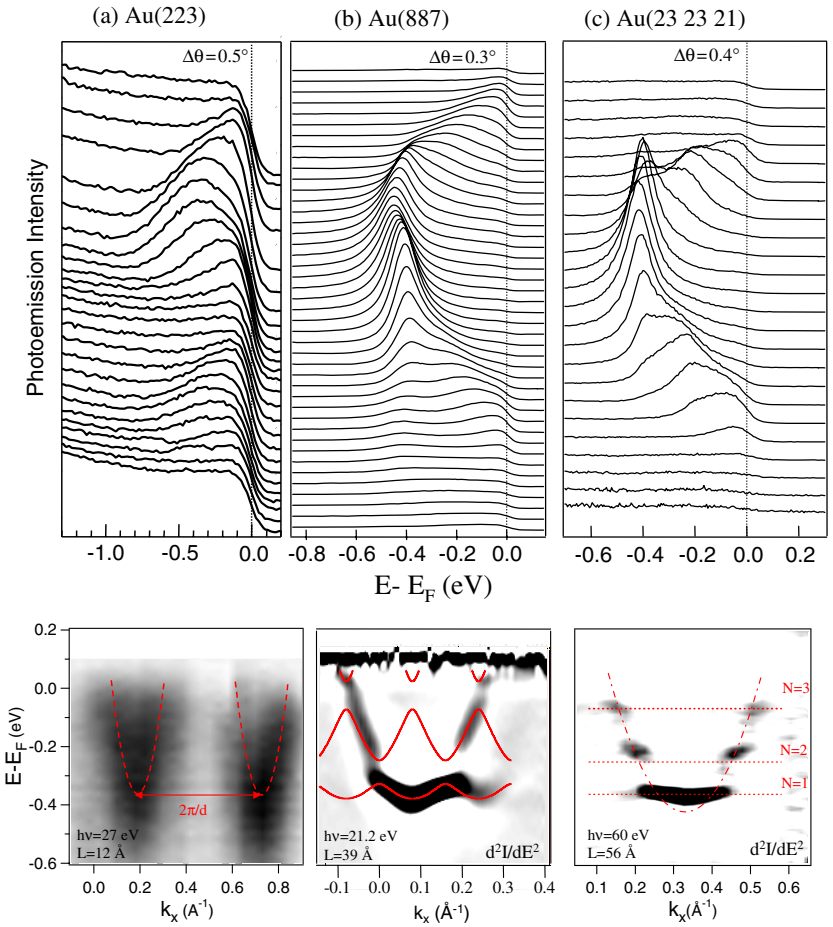

Figure 4. Photoemission spectra for (a) Au(223), $d = 12$ Å, (b) Au(887), $d = 39$ Å, and (c) Au(23 23 21), $d = 56$ Å. Photoemission intensity plots are shown below. For Au(887) and Au(23 23 21) the second derivative in energy is used to enhance peak features.

(EDC) shown on top represent the energy of the surface state relative to the Fermi level for different momentum perpendicular to the steps, i.e., the dispersion of the surface state in this direction. A clear evolution in the dispersion is observed as we vary the terrace size. For small terraces ($d = 12$ Å) we observe two dispersing bands, shifted in energy with respect to the flat surface parabola, and separated by $2\pi/d$, all of them signatures of a 2D superlattice character. The largest terraces ($d = 56$ Å) show a completely different behaviour. The superlattice bands are replaced by non-dispersing energy levels typical of 1D QW states, which can be best seen in the second derivative image plot shown below[5]. The energy levels and their intensity distribution follow the infinite QW behaviour described in the KP model. The broadening of the energy levels can be explained by taking into account the TWD found by STM, as will be shown later. Even if we consider that this broadening contains minibands related to a finite coupling, the minimum value that can be obtained is $U_0 b = 10$ eV Å, which results in $|T_{\mathrm{bb}}|^2 = 0.026$. Thus, we can conclude that these states are uncoupled QW states. In the intermediate regime

[5] The second derivative plots are used to enhance the peak features in the spectra.

($d = 39$ Å), the spectra shows several narrow superlattice bands separated by energy gaps, suggesting a weak but finite transmission through the steps. A similar behaviour has been observed for all other surfaces listed in table 1, their dimensionality depending only on the superlattice periodicity.

The potential barrier U_0b can be generally obtained by fitting the experimental bands to the energy dispersion $E(k_x)$ of equation (1). It is also possible to make a straightforward estimation of U_0b from the (experimental) value of $\Delta E_{\rm bb}$ and assuming $E_{\rm bb}^{U_0b=0}$ from the flat surface [14]. Such a determination of $\Delta E_{\rm bb}$ cannot be done for v-Au(111) surfaces, where terraces reconstruct with different (miscut-dependent) patterns [37], an hence there exists a large uncertainty in the reference energy $E_{\rm bb}^{U_0b=0}$. In any case, the transmission at the band bottom $|T_{\rm bb}|$ is calculated using U_0b and the energy shift $\Delta E_{\rm bb}$. Figure 5 shows the results obtained from the fitting as a function of the superlattice periodicity. For small terraces, U_0b appears to be quite independent on the terrace size, lying between 1 and 2 eV Å. U_0b starts to increase for $d > 30$ Å, exponentially reaching infinity at $d = 56$ Å. In contrast to the sharp evolution of the barrier, the transmission follows a continuous decrease for increasing d. This is due to the double dependency of $T_{\rm bb}$ on U_0b and $\Delta E_{\rm bb}$ mentioned before (see equation (2)). As an effect, even if the potential barriers for $d = 12$ Å and 39 Å are similar, the degree of confinement at the surface band bottom is considerably higher for electrons in the larger terraces.

The regime of small d ($d < 30$ Å) has been studied by several groups for surface states [13, 14, 19, 29] and even for image states [28, 29, 32], finding in all cases similar values of U_0b between 1 and 2 eV Å. The results obtained for surface states are included in figure 5 (white dots). For the intermediate regime (30 Å $< d <$ 40 Å) only two values have reported for U_0b, both being higher than the ones reported here. Shiraki *et al* obtained a barrier $U_0b = 20$ eV Å for Au(887) ($d = 39$ Å) [44], similar to the value found previously by some authors of the present article [17, 25], and higher than the 2.2 eV Å reported here. The discrepancies have been attributed to a lower angular and energy resolution in the former case, which prevents a more careful analysis of the slightly dispersing bands [27]. Notice that U_0b is very sensitive to small differences in $\Delta E_{\rm bb}$, as can be seen in figure 3(b), and hence the latter is not a meaningful number in v-Au(111), where $E_{\rm bb}^{U_0b=0}$ is unknown. For this reason, U_0b for Au(788) has been determined only from the energy gap between the lowest two minibands, which is not sharply defined, and therefore subject to more uncertainties. On the other hand, another group has reported QW states confined by infinite barriers for Cu(665) ($d = 25$ Å) [26]. The strong confinement observed is attributed to localization induced by disorder of the step superlattice. In fact, the broad TWD found in this surface ($\bar{\sigma} = 0.36$) turns the QW spectra into a parabolic feature. In this case a lower electronic coupling through steps induced by lattice disorder could lead to a transition to 1D QW states at smaller d than the one observed in the present work. However, the data in [26] fit only with a 1D QW using a reference energy $E_{\rm bb}^{U_0b=0} = -0.50$ eV, which is remarkably lower than the -0.39 eV measured for the surface band bottom in Cu(111). The authors attributed such difference to a finite transmission of electrons through the steps. Instead, by using their reported band bottom position $E(0) = -0.35$ eV, and $E_{\rm bb}^{U_0b=0} = -0.39$ eV we obtain $U_0b = 1.67$ eV Å and $T_{\rm bb} = 0.35$, which follows the general trend shown in figure 5. In any case, there is a considerable scattering in the whole set of U_0b data in this intermediate regime, suggesting a rather complex 1D–2D transition, where both 1D and 2D states could be coexisting. Indeed, a recent scanning tunnelling spectroscopy (STS) study on v-Cu(111) revealed a mixed 1D and 2D local density of states in this regime [35]. Finally, it is interesting to note that STS experiments on single, isolated terraces [45, 46] demonstrate 1D QW confinement with significant inelastic coupling to bulk states at the steps, but no transmission. As we prove in this work, such terrace confinement can also be observed in step arrays, but with sufficiently large lattice constant.

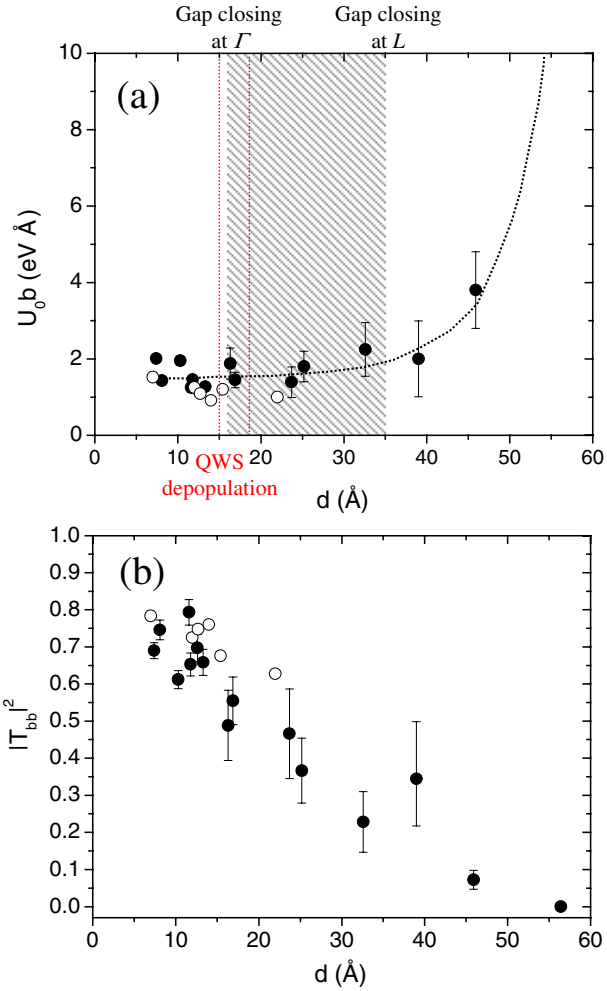

Figure 5. (a) Potential barrier U_0b and (b) transmission probability $|T_{bb}|$ at the band bottom as a function of superlattice periodicity obtained from the fitting of the photoemission spectra with equation (1) (black dots). Values obtained by other groups for $d < 30$ Å are included (white dots). The shadowed area corresponds to the closing of the bulk band gap, and the vertical dotted lines indicate the critical terrace sizes for QW state depopulation in v-Cu(111) and v-Au(111) (see text).

The previous discussion points out the problems of energy resolution and size distribution in averaging techniques such as ARPES in order to achieve a detailed description of quantum size effects in nanostructure arrays. In the case of QW levels, the fact that the intensity distribution tracks the free-electron parabola makes the size distribution problem even more critical. Figure 6 shows a simulation of the photoemission spectra for a surface with $d = 56$ Å and different TWDs assuming that only QW states are present at the surface. The simulation is similar to that of [26]. Image plots for both EDCs along k_x and Fermi surfaces (k_x, k_y plane) are displayed, together with the experimental data. A constant background has been added to account for the inelastic electron contribution, and the EDC curves have been later multiplied by the Fermi Dirac function. A linewidth $\Gamma = 0.125$ eV, obtained experimentally for the $N = 1$ peak, has been used to include lifetime and thermal contributions. The experimental data have

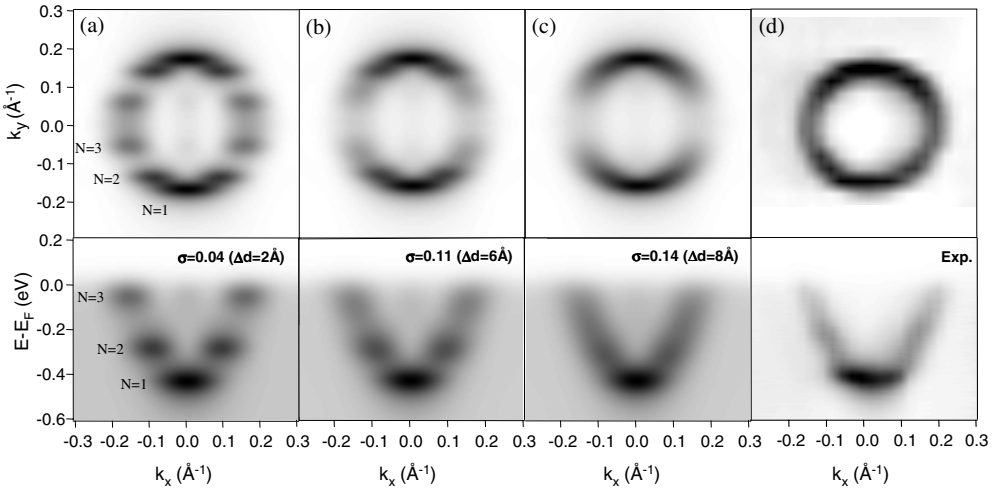

Figure 6. Simulated photoemission spectra and Fermi surfaces from QW states with $d = 56$ Å including a finite TWD. A constant background has been added to account for the inelastic electron contribution, and the EDC curves have been later multiplied by the Fermi Dirac function. A linewidth of 125 meV includes lifetime and resolution. (a) $\bar{\sigma} = 0.04$ ($\Delta d = 2$ Å) (b) $\bar{\sigma} = 0.11$ ($\Delta d = 6$ Å) (c) $\bar{\sigma} = 0.14$ ($\Delta d = 8$ Å). (d) Experimental data for Au(23 23 21), with $d = 56$ Å.

been shifted along k_x by $2\pi/d$, in order to bring them inside the first superlattice Brillouin zone. For $\bar{\sigma} = 0.04$ ($\Delta d = 2$ Å), the QW levels are easily distinguishable. In the Fermi surface, they form lines along k_x modulated in intensity. For $\bar{\sigma} = 0.11$ ($\Delta d = 6$ Å), the STM experimentally measured value, the QW levels get broader, and for $\bar{\sigma} = 0.14$ ($\Delta d = 8$ Å) the spectra look more a dispersing parabola rather than a set of non-dispersing levels. In the Fermi surface (FS), the lines have been transformed into a single 2D ring. Our experimental data seem to lie between the last two examples, suggesting a slightly larger TWD than the one measured by STM. The broadening of the energy levels originated from the TWD can account for the broad features observed in the spectra of figure 4(c) for $d = 56$ Å. This analysis demonstrates how critical a sharp TWD can be to appropriately study electronic states in more complex lateral nanostructures by averaging, spectroscopic techniques.

Wavefunction properties of surface electrons can be further analysed with photon energy-dependent photoemission. In 1D QW states, the photoemission intensity has been shown to be proportional to the probability density in reciprocal space, such that phase-recovery techniques can be applied to obtain the real space wavefunction [25]. In all 1D and 2D states one can determine the symmetry of the wavefunction in the k_z–k_x plane by varying the photon energy and hence sampling the broad momentum distribution (see the rod in figure 9) in the direction perpendicular to the surface [25]. Such analysis is shown in figures 7 and 8. The evolution of the spectra with varying photon energy can be best followed by plotting the 2D FS in the surface plane (k_x, k_y). Figure 7 displays the FS for representative cases in the two regimes, Cu(335) with $d = 9$ Å and Au(23 23 21) with $d = 56$ Å. In both cases we observe a pair of rings separated by $2\pi/d$ umklapp vectors, and modulated in intensity as we vary the photon energy. For the 2D superlattice state, the FS has a ring shape, with slight k_x–k_y distortion due to the different effective mass of the electron perpendicular and parallel to the steps. As explained before, the ring-like shape of the FS for Au(23 23 21) is an effect of the finite TWD, which makes the set of 1D QW straight lines merge into a circle.

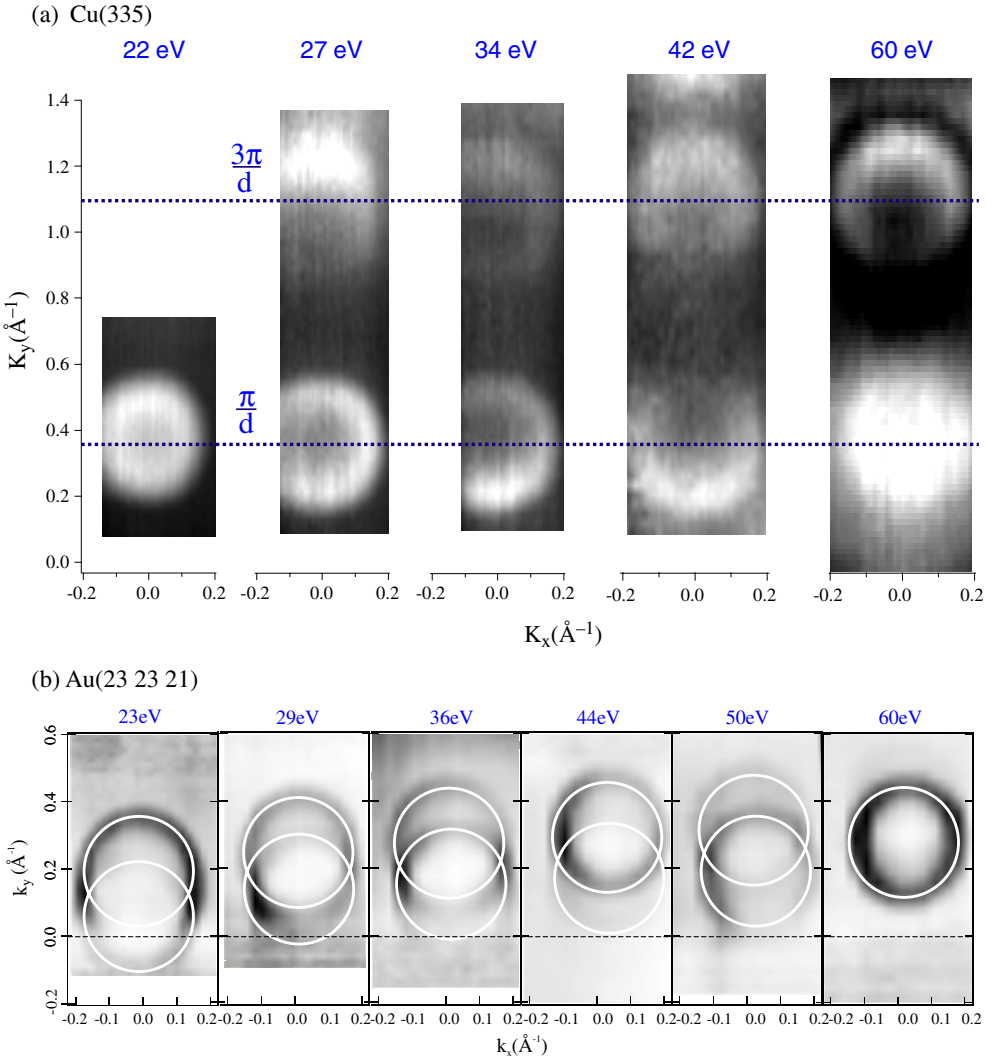

Figure 7. Fermi surfaces of (a) Cu(335), $d = 9$ Å and (b) Au(23 23 21), $d = 56$ Å for different photon energies.

Since the surface state in Au(23 23 21) is confined within terraces, the umklapp bands observed in figure 7(b) can only be explained by photoemission final state effects, i.e., it would be originated by step lattice diffraction of the outcoming photoelectron beam, similar to LEED. For 2D superlattice bands, both initial (surface) state superlattice folding and final state diffraction effects might contribute. Since there is no shift in the k_y direction, we can analyse the data by drawing the centre of these rings in the (k_z, k_x) plot shown in figure 8. k_z is obtained from the photoelectron kinetic energy, assuming free-electron-like final states with inner potentials $V_0 = 13.5$ and $V_0 = 15.2$ eV for Cu and Au, respectively [25]. The data for Cu(335) line up perpendicular to the average surface, defined macroscopically by the vicinal surface. The rod formed by the data represents the broad spectrum in the direction of the decay into the bulk, indicating that the 2D superlattice state propagates along the average

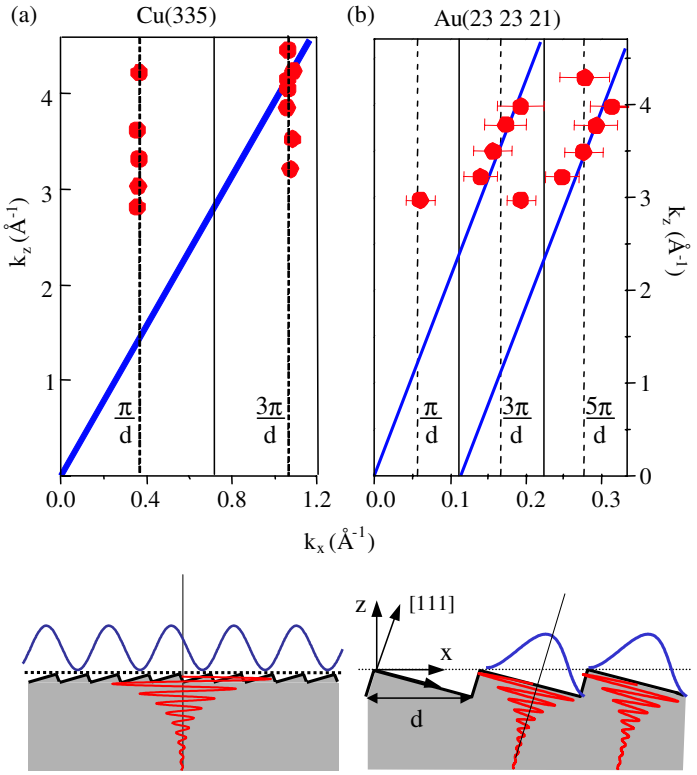

Figure 8. (k_z, k_x) plots for the centre of the Fermi surfaces of (a) Cu(335), $d = 9$ Å and (b) Au(23 23 21), $d = 56$ Å for different photon energies. A schematic description of the wavefunctions derived from this analysis is shown below.

surface. Instead, the data for Au(23 23 21) show a decay into the bulk perpendicular to the (111) terraces, indicating that in this case the symmetry plane is rather defined by the (111) plane, as expected for QWs confined within the terrace. A schematic description of the wavefunction in each case is shown in figure 8.

In summary, the behaviour of the potential barrier as a function of the step superlattice periodicity distinguishes two completely different regimes: for small terraces the 2D superlattice state interacts with a rather weak potential barrier and propagates along the average surface, while for large terraces decoupled 1D QW states are found confined within the terraces. The two regimes are connected by a continuous, smooth transition. The origin of this transition has been extensively discussed in previous works [16, 25–27, 34]. As mentioned before, QW states were found by Baumberger *et al* on a v-Cu(111) with a lattice parameter $d = 25$ Å. The d-dependent transition from 2D states to 1D states was attributed to localization induced by step lattice disorder, which inhibits coherent coupling of electrons through adjacent steps. They related the higher disorder at 25 Å to the proximity of this vicinal surface to more stable terrace sizes around $d = \lambda_F/2 = 15$ Å, where the total electron energy is lowered by opening a gap at the Fermi level [26]. Morgenstern *et al* observed a depopulation of the QW states at $d = \lambda_F/2$ by STS, where λ_F is the Fermi wavelength [34][6]. At this terrace size the lowest QW

[6] Band-gap opening at the Fermi level and QW state depopulation are not related phenomena, even if the critical terrace sizes appear to be the same.

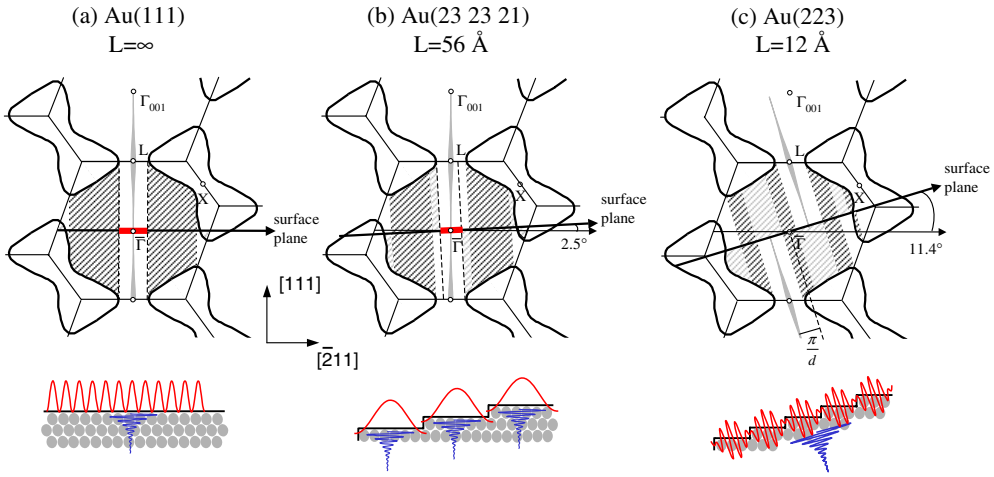

Figure 9. Schematic projection of bulk bands at the energy of the band bottom of the surface state for vicinal surfaces with increasing miscut angles α. The $\bar{\Gamma}$ gap of the flat surface in (a) shrinks in (b) and has already vanished in (c). The reducing size of the gap give rise to a progressive surface–bulk band overlap along the ΓL line, where surface states of the band bottom are located. The light grey, cigar-shaped rods represent the broad momentum distribution due to surface confinement.

level crosses the Fermi energy. For $d < \lambda_F/2$ one-dimensional QW states were replaced by 2D superlattice states, therefore the QW state depopulation was related to such a transition. These effects might contribute to the transition, but they cannot explain the decrease in the potential barrier observed for decreasing d. By contrast, the progressive mixing of surface and bulk states occurring in vicinal surfaces with increasing miscut (decreasing d) can qualitatively explain the reduction in the step potential [16, 27, 25]. Indeed, a significant mixing with bulk states around step edges has recently been found for surface states at vicinal surfaces [47]. This mixing would result in a larger penetration of the surface state and therefore a weaker interaction with the step potential, leading to a smaller effective potential $U_0 b$. A similar behaviour was found for image states at v-Cu(111) and v-Cu(100) surfaces, which display an increasing sensitivity to the step potential barrier as they get physically closer to the surface [31, 29]. With the aim of estimating the different penetration length of the surface state wavefunction inside the bulk for 1D and 2D states in v-Cu(111), a comparative photon energy-dependent intensity analysis has been made for Cu(111) and v-Cu(111) [26, 23]. Such intensity peaks around $h\nu = 67$ eV, where one probes the L point of the bulk band structure. Ideally, the width of this cross section peak is inversely proportional to the penetration length, but no significant differences have been found between flat and vicinal surfaces. This can be explained by the fact that the 67 eV resonance is dominated by final-state wave vector broadening contributions, and also shaped by final state band structure effects, thereby limiting the accuracy of such a comparative analysis [21, 48].

The progressive surface–bulk mixing as the superlattice periodicity decreases is qualitatively explained using the bulk projection diagram shown in figure 9. The bone-shape features (thick lines) represent (k_z, k_x) cuts of constant energy for the bulk bands at the energy of the band bottom of the surface state, similar to the bulk Fermi surface at the Fermi level. Bulk states project on the surface plane, which is represented by the nearly horizontal line that rotates with the miscut angle. Along this plane, regions of the surface Brillouin zone (SBZ) where the bulk bands are projected from both sides of the constant energy contour are shadowed in black, whereas regions that are projected only from one side are shadowed in light grey. The gap left

Table 2. Values for the critical lengths for QW state depopulation ($\lambda_F/2$), complete closing of the gap for the band bottom ($d_c^{\Gamma L}$), and closing of the gap for the band bottom at the L point (d_c^L).

	$\lambda_F/2$	$d_c^{\Gamma L}$ (Å)	d_c^L (Å)
Cu	15	17	33
Au	18	18	35
Ag	37	21	42

around $\bar{\Gamma}$ is represented by a thick line. The L point projection marks the edge of the SBZ at $\pm\pi/d$. As mentioned before, the 2D character of the surface states results in a broad spectrum along ΓL with the intensity centred at L, represented by cigar-shaped rods. The key point is the overlap between the surface state Fourier components along the ΓL line and projected bulk states at the same energy. On the flat surface of figure 9(a) the bulk projection leaves a gap at $\bar{\Gamma}$, where the entire surface state Fourier spectrum is found. By changing the miscut angle, the surface plane rotates and hence the band projection along the SBZ. For small miscut angles, the projected bands do still not overlap with the surface state Fourier spectrum, and hence the surface state, highly localized on the surface, will interact with a large effective step barrier, similar to that of isolated steps in the flat surface. This is the case for Au(23 23 21), as shown in figure 9(b). For larger miscut angles, as the projected band gap shrinks, there is an increasing overlap of projected bulk states with surface state Fourier components from L to Γ. At a certain miscut, the gap vanishes and the overlap is complete; hence the surface state becomes a resonance, as shown in figure 9(c) for Au(223). Since the spectral distribution of the surface state is centred around the L point, the surface–bulk overlap at this point will be the most important in order to determine the critical terrace size for the transition. The critical terrace sizes d_c^L for surface–bulk mixing at the L point are given in table 2 for the band bottom. Interestingly, these values are close for the three noble metals, indicating a similar transition regime. The 1D to 2D transition observed agrees well with d_c^L, as can be seen in table 2 and in figure 5(a), where the shadowed region indicates the surface–bulk mixing regime. Note that d_c shifts to larger values for energies above the band bottom, explaining why we already see a decrease in the barrier for $d = 45$ and 39 Å. The d-dependent, progressive surface–bulk mixing, and the corresponding change in the transmission coefficient, suggests a smooth 1D–2D transition.

The reason why the QW state depopulation has only been observed in Ag(111) can also be explained with the surface–bulk mixing model. The values for $\lambda_F/2$ for the three noble metals are included in table 2. For Cu(111) and Au(111), $\lambda_F/2$ lies below d_c^L, but for Ag(111), $\lambda_F/2$ is very close to d_c^L. This means that in Ag, the depopulation of QW states occurs just when the mixing with bulk states starts to be important, and therefore can still be observed. On the other hand, in Cu and Au the transition to 2D occurs before reaching the critical terrace size for surface state depopulation, and hence the QW state is effectively suppressed before depopulation occurs.

So far we have seen how the effective potential barrier at steps can be modified by varying the miscut angle of a vicinal surface. But the barrier can also be modified by changing the chemical nature of the steps, for example, by step decoration with different elements. The step decoration might lead to both increase or reduction of the step barrier [40, 32, 44], or can even induce a sign inversion [20], where repulsive barriers become attractive. Thus, tailoring the step barrier by step decoration appears a simple way to tune the electronic structure in the step array, i.e., a handy way of creating nanostructures with different electronic properties without changing the building-block nano-object.

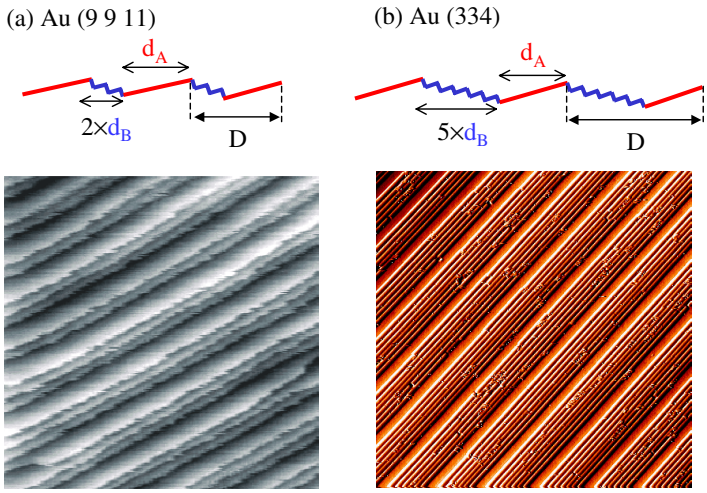

Figure 10. STM images of two faceted vicinal surfaces. (a) Au(9 9 11), size: 50×50 nm^2 (courtesy of V Repain). (b) Au(334), size: 200×200 nm^2. The schematic surfaces above indicate the relevant parameters.

4. Periodically faceted Au(111) surfaces

The Au(111) surface presents a $22 \times \sqrt{3}$ superstructure induced by a herringbone-like reconstruction that alternate fcc and hcp areas. On vicinal surfaces the steps influence the reconstruction by changing its periodicity and direction [37]. Moreover, this reconstruction appears to be the reason for the high stability of the step array in single-phase Au(111) vicinals, which indeed display much sharper step lattices than Cu(111) vicinals. For miscut angles beyond $\sim$4° and below $\sim$10°, the fcc/hcp reconstruction triggers periodic faceting with two stable phases, i.e., two different terrace sizes [37]. Figure 10 show STM images of two faceted v-Au(111) surfaces together with their schematic side view description, indicating the relevant parameters. The values for the step and the stripe periodicities are listed in table 3. Interestingly, the terrace size in each of the phases is the same for the two vicinals. Both exhibit a single large terrace of $d_A \approx 41$ Å (phase A) and step bunches with relatively small terraces $d_B = 14$ Å in between (phase B). The only difference between Au(9 9 11) and Au(433) is the number of $d_B = 14$ Å wide terraces, i.e., the stripe width of phase B. Au(9 9 11) has two terraces in phase B, whereas Au(334) has five. Consequently, the total periodicity $D = w_A + w_B$ and the relative weight of the phases will also be different for each surface. On the other hand note that $d_A \approx 41$ Å and $d_B = 14$ Å represent characteristic terrace size values for both the 1D QW state regime and the 2D superlattice regime, which are then expected to interact in the faceted surfaces of figure 10.

Figure 11(a) shows the characteristic EDC photoemission spectra for Au(9 9 11), measured with $h\nu = 17$ eV. We may distinguish two different kinds of feature: a sharp non-dispersing peak at -0.41 eV and two broader bands dispersing across the Fermi energy, with a clear energy gap between both. As deduced from the photon-energy-dependent photoemission intensity analysis of figures 11(b) and 12, such distinct features are connected to the local modulation of the surface wavefunction on each of the phases. The analysis is compatible with the wavefunction model sketched in figure 13, which assumes two different states, one for each phase.

In figure 11(b) we show the photoemission intensity plots taken at different photon energies, where we distinguish both the very intense non-dispersing peak of figure 11(a), as

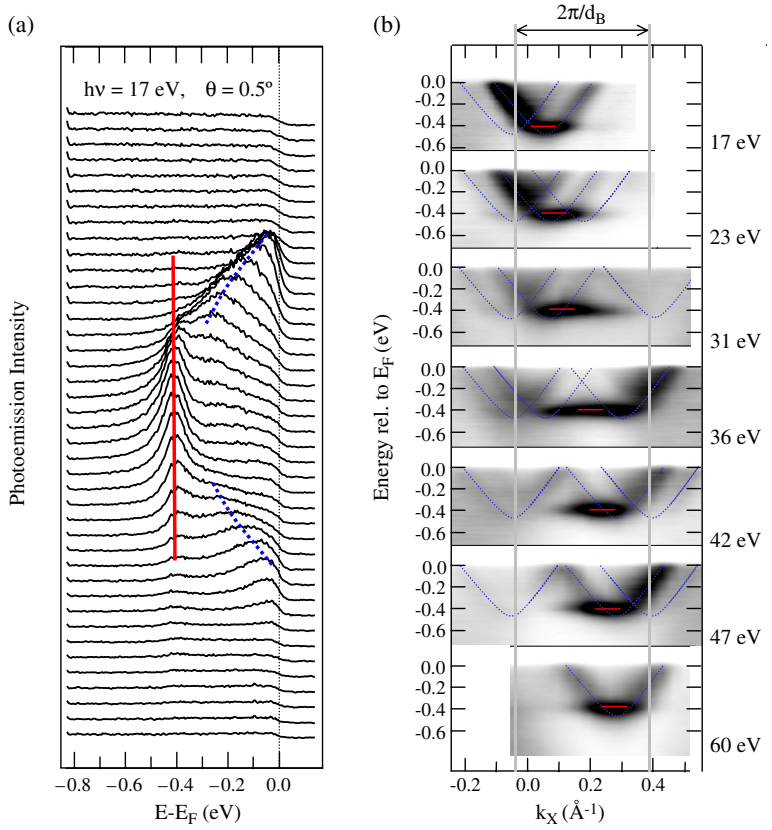

Figure 11. (a) Photoemission spectra for Au(9 9 11) at 17 eV, where a non-dispersing level is followed with a horizontal solid line. (b) Image plots of the photoemission intensity at different photon energies. The different dispersing branches have been grouped with distinct umklapp parabolas (dotted lines). The lateral shift of the non-dispersing level is followed with a solid line. The vertical lines are guide lines that mark the intensity maxima in the dispersing features.

Table 3. Structural parameter list for the faceted vicinal surfaces Au(9 9 11) and Au(334). The values are obtained from an STM image analysis [37]. d_A corresponds to the terrace width for the large terrace phase (phase A), and d_B for the small terrace phase (phase B). The number of terraces in each stripe is indicated in parentheses. D is the total periodicity of the faceted structure, and α the miscut angle.

Vicinal index	Step-type	d_A (Å) (no. terraces)	d_B (Å) (no. terraces)	D (Å)	α (deg)
Au(9 9 11)	{100}	42.0 (×1)	14 (×2)	70	5.6
Au(334)	{100}	40.0 (×1)	14 (×5)	110	8.1

well as the dispersing features, the latter exhibiting umklapp with $2\pi/D$ superlattice vectors. Leftward and rightward dispersing branches in figure 11(b) have been grouped with a set of umklapped, free-electron-like parabolic envelopes, shown with dotted lines. These parabolas can be viewed as $2\pi/D$ diffraction cones that contain the most intense (closest to the cone) superlattice minibands, in the same way as the diffraction cone in figure 3(a) (thick parabola) marks the step lattice minibands which are observed in single-phase vicinals (plotted with thicker dotted lines in figure 3(a)). The intensity distribution reflects a complex Fourier

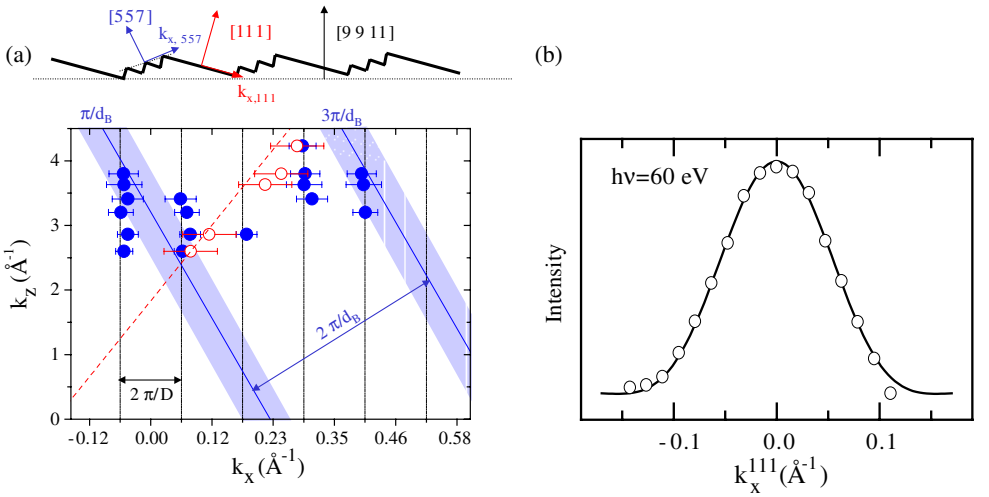

Figure 12. (a) (k_z, k_x) plot for the band bottom of the dispersing features (filled dots) and for the centre of the non-dispersing line (open dots) observed in figure 11(a). The data for the dispersing features, separated by the superlattice wave vector $2\pi/D$, line up perpendicular to the average surface. The data for the non-dispersing feature follow a $-4\pi/D$ umklapp line of the (111) direction. (b) Photoemission intensity of the 1D QW level as a function of the momentum perpendicular to the steps in phase A. The data are fitted with the Fourier transform of the QW state of an infinite well of size $d = 42$ Å [22].

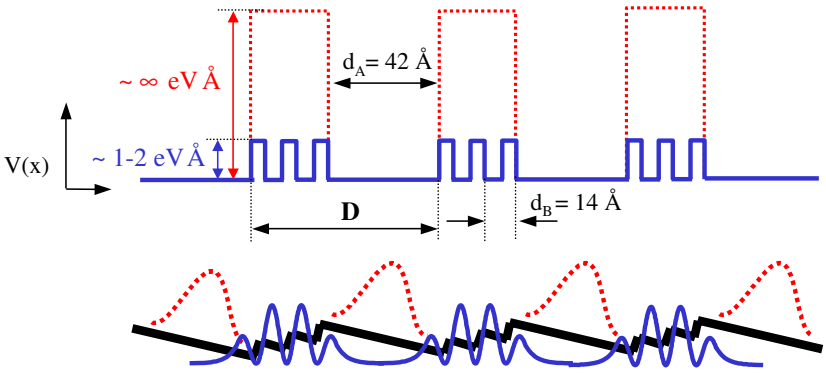

Figure 13. Surface state wavefunction description for Au(9 9 11). Two non-overlapping states characterize each of the phases, namely a quasi-1D state in large terraces, and a 2D extended state highly localized in step bunches.

composition of the surface state wavefunction, which is rationalized in the (k_z, k_x) plot of figure 12(a). In this figure, filled dots correspond to the bottom of the parabolic envelopes for different photon energies. In the same way as the 2D states in figure 8, the different sets of points, separated by $2\pi/D$ vectors, line up in the direction perpendicular to the surface, proving that the dispersing band in figure 11(a) belongs to a surface state that propagates across the average (9 9 11) surface plane.

As a function of photon energy, one can observe in figure 11(b) an abrupt shift in the intensity maximum for the dispersing features, from a leftward branch at ~ -0.05 Å^{-1} to a rightward branch at ~ 0.4 Å^{-1} (indicated by vertical thick lines). Such a jump corresponds

to $2\pi/d_B = 14$ Å, i.e., the size of the small terraces of figure 10. Such behaviour can be explained by considering that the wavefunction is highly localized in phase B stripes and modulated by the local step lattice. The situation is analogous to the 2D confinement of surface states in the direction perpendicular to the surface [49], or quantum well states in a thin film [50]. The wavefunction is modulated by the atomic planes in the substrate, giving rise to a spectral distribution along k_z, which, in the case of surface states periodically peaks at $k_z = (2n+1)\pi/d_z$, where d_z is the spacing between the atomic planes. This momentum distribution gives rise to the intensity modulation sampled by the photon-energy-dependent analysis of figures 7 and 8. In the same way, a wavefunction laterally localized in stripes of phase B and modulated by the step lattice with period d_B gives rise to a momentum distribution parallel to this step lattice peaking at $(2n+1)\pi/d_B$. In fact, if we plot in figure 12(a) the momentum direction for the π/d_B and $3\pi/d_B$ parallel to the surface in phase B, we see that the intensity maxima observed in figure 11(b) follow these lines. Thus, we conclude that the dispersing features of figure 11 belong to 2D surface electrons with higher probability density located in phase B, as sketched in figure 13. A similar analysis can be done for the non-dispersing feature by plotting the centre of its intensity distribution along k_x, shown with open dots in figure 12(a). In the analysis we omit the points for 31 and 36 eV photon energy, where final state umklapping broadens the intensity distribution. Similar to the k_x–k_z plot of the 1D QW in Au(23 23 21) shown in figure 8(b), data points for the non-dispersing peak in Au(9 9 11) follow a $-4\pi/D$ umklapp line parallel to the [111] direction, reflecting the terrace confinement and 1D QW-like character of this peak.

In figure 12(b) we analyse the photoemission intensity distribution of the non-dispersing peak as a function of $k_{x,111}$, the momentum perpendicular to the steps in the reference plane of phase A, with $h\nu = 60$ eV. The k_x scale has been shifted by $2\pi/D$. At $h\nu = 60$ eV we find a single umklapp parabolic envelope [25], such that the intensity plot shown in figure 12(b) directly probes the lateral extension of the surface wavefunction for the 1D QW state [22]. In fact, the photoemission intensity is proportional to the probability density of the wavefunction in reciprocal space, which can be expressed as

$$I_{QW_\infty}(k_{x,111}) \propto \frac{1-(-1)^N \cos(k_{x,111}\cdot d)}{\left[(k_{x,111})^2 - (\frac{\pi N}{d})^2\right]^2} \times N^2 \tag{4}$$

where d is the width of the QW and N the quantum number of the wavefunction. The solid line in 12(b) represents the spectral intensity expected for the lowest $N = 1$ level in the infinite QW of size $d = 42$ Å, the size of the large terrace in Au(9 9 11). Thus, we conclude that the probability density in the lowest, non-dispersing electronic state of figure 11 is mostly located within the large terraces, as shown in the wavefunction model of figure 13. The higher lateral localization found in these terraces in comparison to the 39 Å wide terraces of Au(887) could be due to the fact that in the faceted surface the large terraces are separated by stripes of phase B, inhibiting a coherent coupling through terraces.

5. Striped Ag/Cu heterostructures

Self-assembled heterogeneous striped structures can be created by depositing Ag on selected v-Cu(111) [51–53]. The driving force for faceting in this case is the stress relief caused by lattice matching of the Ag layer with a particular substrate orientation. By choosing a vicinal surface with high step density we facilitate the formation of facets with better lattice matching in the direction perpendicular to the steps. In particular, the Ag layer likes the (112) orientation, which is vicinal to the [111] direction with a very high step density. If the original vicinal

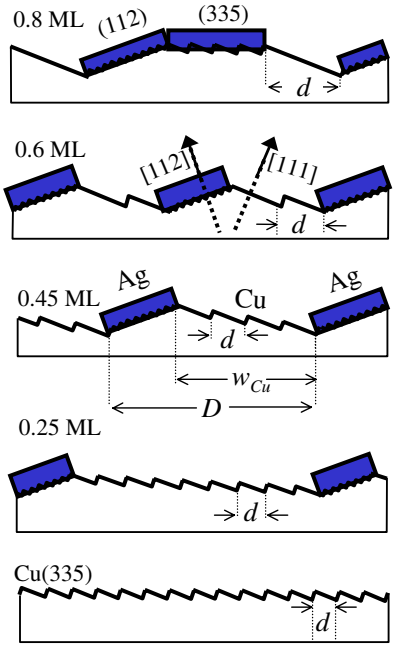

Figure 14. Schematic side view evolution of the striped pattern induced by Ag on Cu(335) with Ag coverage (Θ).

substrate has a lower step density than the (112)-plane, Ag-induced faceting results in a one-dimensional striped structure with (112)-oriented, Ag-covered facets and clean Cu stripes with a reduced step density with respect to the substrate plane. Thus, increasing the Ag coverage results in a continuous increase of the terrace size in the bare Cu phase. Here, like in faceted vicinal Au(111), the elastic interaction between the phases induces periodic striped patterns of Ag-covered and clean Cu domains.

The evolution of the striped pattern as a function of Ag coverage is schematically represented in figure 14. STM images for three different thicknesses (Θ) are shown in figure 15. The images are shown in the derivative mode in order to enhance the difference between the phases. Dark areas represent Ag covered stripes whereas brighter areas are bare Cu stripes. The insets show a closer view of both phases: the Ag stripes forming a Moiré pattern, and the Cu stripes with monatomic steps. Close-packed Ag layers grow on (112) facets up to $\Theta = 0.64$ ML, the point where Cu stripes become a single 36 Å wide Cu terrace. Below the critical coverage $\Theta = 0.64$ ML, the widths of Cu and Ag stripes can be varied smoothly in the 30–300 Å range by simply tuning the Ag coverage. The decrease in the Cu stripe size is accompanied by a continuous increase of the terrace size inside the stripe from 10 to 36 Å. The TWD measured at the Cu stripes is close to the ones measured at the corresponding single-phase vicinals. Beyond $\Theta = 0.64$ ML, the Ag covered facets change gradually from (112) to (335), although the Cu stripe width remains constant at 36 Å. As the coverage increases, contiguous stripes begin to coalesce, such that the total area of the 36 Å wide Cu terraces shrinks and eventually reduces to zero at 1 ML [54]. A mixture of (112) and (335) facets in this transition regime can be seen in the inset of figure 14(c), where $\Theta = 0.85$ ML. A similar stripe evolution has been observed for Ag deposited on Cu(223) [51, 53]. As can be noted, the striped surface is an interesting 1D analogue to the 2D superlattice heterostructure, where surface stripes would be viewed as '1D thin films' forming an infinite superlattice.

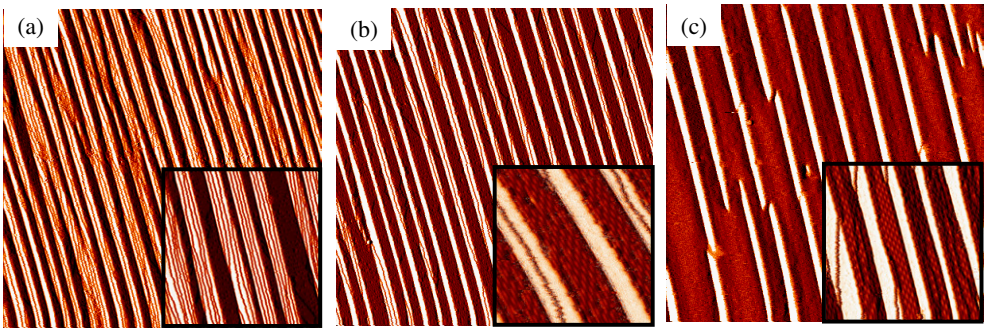

Figure 15. STM images (100×100 nm^2) obtained at different Ag coverage (Θ) showing different striped structures. The insets show a detailed view of the corresponding Moiré pattern in each structure: (112) facets in (a) $\Theta = 0.34$ ML and (b) $\Theta = 0.50$ ML, and a mixture of (112) and (335) facets in (c) $\Theta = 0.85$ ML.

In figure 16 we show the photoemission spectra and Fermi surfaces for Ag-induced stripes on Cu(335) as a function of coverage, measured at $h\nu = 22$ eV. The surface states split into distinct Ag-like states (dashed lines), and Cu-like states (solid lines). The former is located above E_F for (112)-covered facets and $\Theta < 0.64$ ML and cannot be observed. The Cu state feature exhibits a clear transition from a 2D-like dispersing band to a 1D-like non-dispersing peak as we increase the Ag coverage, i.e., as we decrease the terrace size d inside the Cu nanostripe. Furthermore, for small d, umklapp superlattice bands with $2\pi/d$ wavevectors can be observed for 2D states at higher photon energies [48]. Figure 16(b) shows the evolution of the Fermi surface as a function of coverage with more detail. The 2D-like ring observed for clean Cu(335) increases its diameter as we increase d, a signature of the downwards energy shift in the surface band. In addition, as the coverage increases, the ring-like shape continuously stretches along k_x, becoming a single straight line along k_x for $\Theta = 0.6$ and 0.8 ML, characteristic of a single 1D QW level. At this coverage, we can observe a very intense ring-like structure around $k_x = 0.3$ Å^{-1}. This remains as the unique feature in the fully covered surface and, hence it can be associated to surface states in (335)-oriented Ag covered stripes. Although the dispersing Ag state is marked in the EDC curves of figure 16(a) for 0.8 ML, the band minimum cannot be accurately determined, since the peak is considerably cut-off by the Fermi edge. On the other hand, the absence of any remarkable Ag state intensity for (112)-oriented stripes at low coverage is expected from the higher density of steps of the (112) plane, which shifts the surface band by about 100 meV with respect to the (335) plane [40].

In any case, the interesting feature, undergoing a change in dimensionality, is the one derived from Cu stripes with varying d. The finite size of the stripe is reflected in the small shift of the surface state with respect to infinite vicinals with the same d, as shown in figure 17. Here we represent the energy shift of the band bottom (or the $N = 1$ QW position) as a function of terrace width. The total width of the Cu stripe ω_{Cu} in each case has been included in the x scale. For comparison, we have included the energy shifts obtained in single-phase vicinals with varying d (solid line). As it can be observed, the data points follow the trend of the single-phase surfaces for small terraces, but large ω_{Cu}. As we increase d, the stripe width is decreased and the data points start to deviate from their respective single-phase surfaces. On the other hand, we see that the data in this range follow nicely the energy shift produced by an infinite QW of size ω_{Cu} (dashed line). In fact, in this range the Cu stripes do not contain steps anymore, so no contribution from the step lattice is expected. The schematic surface wavefunction arising

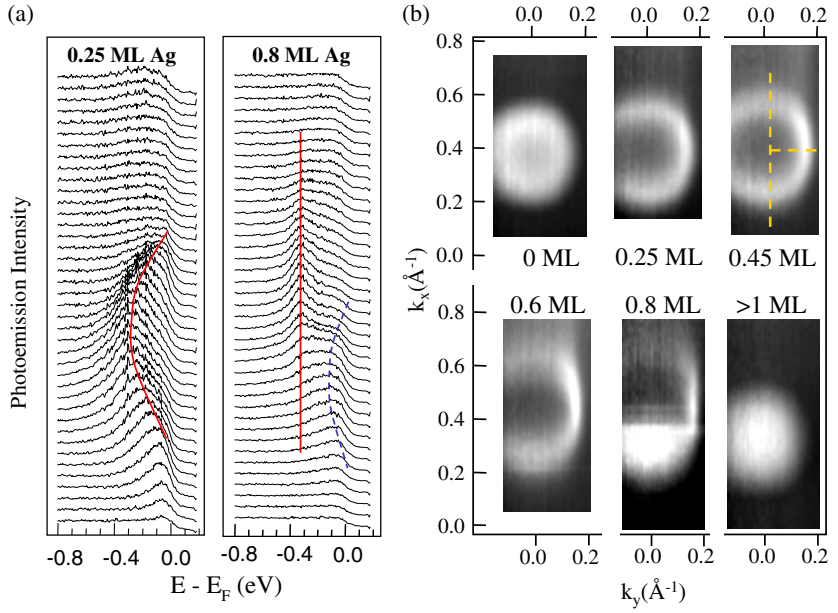

Figure 16. (a) Photoemission spectra from Ag-induced stripes in Cu(335) for $\Theta = 0.25$ and 0.8 ML. The feature related to bare Cu stripes is indicated by a solid line, whereas dashed lines follow the feature related to Ag covered stripes. (b) Fermi surfaces for the same system for increasing Ag coverage.

from this analysis is depicted in figure 17 (right). Monatomic steps within the Cu stripe form an array of weak potential barriers of 1–2 eV Å, surrounded by infinite potential barriers at the stripe boundaries. For Ag-induced stripes on Cu(223) a smooth 2D–1D transition is observed at $d = 30$ Å, where Cu stripes become single terraces [48]. Notice from figure 17 that the Cu stripe width ω_{Cu} for a terrace size of the order of the critical size d_c^L is very small, an hence the transition observed for the step barrier with single-phase vicinals is obscured by the influence of the new (infinite) potential barrier at stripe boundaries, which actually drives the 2D–1D transition in Cu nanostripes.

The finite size of the stripe also reflects in momentum space as a broadening effect, as expected from Heisenberg's principle [55]. This can be observed in the FS shown in figure 16(b). In the direction perpendicular to the steps (k_x) the ring becomes broader as we decrease the size of the Cu stripe by increasing the coverage. The increased broadening is a signature of a smaller spatial distribution of the wavefunction, i.e., a smaller size of the confining well. On the other hand, in the direction parallel to the steps (k_y) the evolving feature becomes sharper for increasing coverage. The latter is a consequence of an enhanced lifetime due to the decreasing step density in each stripe, i.e., a narrower peak in the EDC due to a smaller lifetime broadening leads to a narrower line in the FS. Since both lifetime and TWD broadening effects will contribute in a similar way in the FS along both k_x and k_y [55], the asymmetry $\Delta k_{xy} = \Delta k_x - \Delta k_y$ will be directly related to quantum size effects along k_x. In figure 18 we plot Δk_{xy} as a function of Ag coverage and the corresponding stripe width ω_{Cu}. The broadening Δk_x (Δk_y) is measured at $k_y = 0$ ($k_x = 0$), as indicated by the dashed lines in figure 16(b). Note that, for $\Theta > 0.64$ ML, $\omega_{\mathrm{Cu}} = 36$ Å is constant. As mentioned in the previous section, the broadening along k_x due to an infinite quantum well of width ω_{Cu} is proportional to the probability density of the wavefunction in reciprocal space, and follows

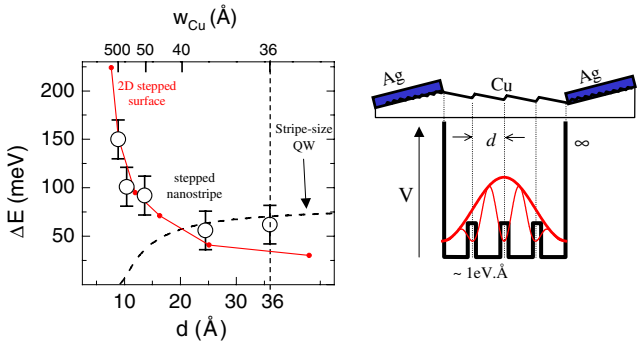

Figure 17. Energy shift of the surface states as a function of terrace size and Cu stripe width w_{Cu}. The energy shift for single-phase vicinals are plotted with dots and lines. The dashed line corresponds to the energy shift for total confinement in the infinite quantum well of size w_{Cu}. The schematic drawing on the right represents the array of potential barriers on the Cu stripe and the resulting $N = 1$ wavefunction.

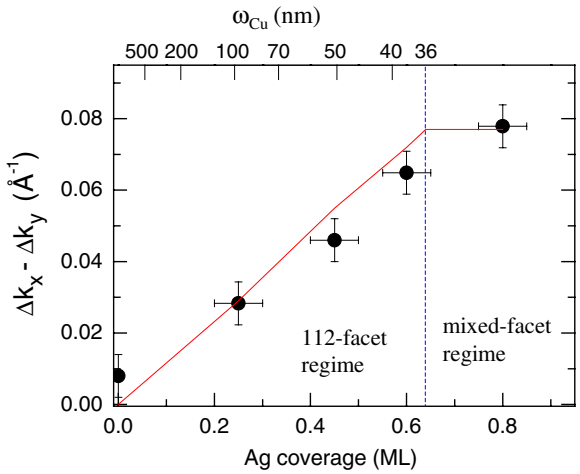

Figure 18. Asymmetry in the Fermi surface broadening $\Delta k_x - \Delta k_y$ as a function of Ag coverage. The corresponding stripe width ω_{Cu} is indicated above. The broadening due to infinite quantum well confinement within ω_{Cu} stripes is represented with a solid line.

the expression of equation (4). This expression leads to the peaks in the momentum intensity distribution observed for the QW states Au(23 23 21) in figure 4(c). Interestingly, the width of the peaks for $N > 1$ is independent of N, and hence it only depends on ω_{Cu}. Moreover, the intensity along k_x at $k_y = 0$, used to calculate Δk_x, is a contribution of QW with $N > 1$, as can be observed in figure 6. Therefore, one can use the broadening (HWHM) obtained from equation (4) for $N > 1$ as a measure of the broadening produced by the confinement on the stripes. This is represented by a solid line in figure 18. The good agreement between the data points and this curve indicates that confinement at the stripes accounts for the momentum broadening observed in the data.

6. Summary

In this review the electronic structure of different type of vicinal surfaces has been extensively studied. In the most simple case of single-phase surfaces, a detailed analysis leads to the

observation of a smooth transition from 1D QW states to 2D superlattice states as the terrace size is decreased. This transition is explained in terms of mixing with bulk projected states. The relevance of good size distribution and experimental resolution for studying the dimensionality of the electronic states with averaging techniques such as ARPES has been discussed.

For double-phase surfaces more complex electronic structures have been observed. In Au(9 9 11) coexisting 2D and 1D states have been observed. While the 1D state is confined in one phase, the 2D state seems to propagate along the whole surface. In the case of the Ag-induced striped surfaces in v-Cu(111), strongly localized states have been found in each phase. The electronic phase separation, together with the periodicity of the stripes makes this system very attractive for further applications in selective adsorption, growth of nanostructures or photonic devices.

Acknowledgments

This work was supported by the Spanish Ministerio de Ciencia y Tecnología (MAT-2002-11975-E, FIS2004-06490-C03-03), the Basque Country government Scholarship BFI 04.313.R2, and as part of the European Science Foundation EUROCORES Programme SONS and a Marie Curie Intra-European fellowships within the 6th European Community framework programme. The SRC is funded by the National Science Foundation (Award No. DMR-0084402). Experiments performed at LURE were funded by the Large Scale Facilities program of the European Union. Technical support from the Spanish–French beamline staff and the use of the photoemission spectrometer at the University of Technology Dresden are gratefully acknowledged.

References

[1] Gambardella P, Dallmeyer A, Maiti K, Malagoli M C, Eberhardt W, Kern K and Carbone C 2002 *Nature* **416** 301
[2] Repain V, Baudot G, Ellmer H and Rousset S 2002 *Mater. Sci. Eng.* B **96** 178
[3] Kuntze J, Mugarza A and Ortega J E 2002 *Appl. Phys. Lett.* **81** 2463
[4] Crain J N, McChesney J L, Zheng F, Gallagher M C, Snijders P C, Bissen M, Gundelach C, Erwin S C and Himpsel F J 2004 *Phys. Rev.* B **69** 125401
[5] Ma X, Meyerheim H L, Barthel J, Kirschner J, Schmitt S and Umbach E 2004 *Appl. Phys. Lett.* **84** 4038
[6] Pratzer M, Elmers H J, Bode M, Pietzsch O, Kubetzka A and Wiesendanger R 2001 *Phys. Rev. Lett.* **87** 127201
[7] Frohn J, Giesen M, Poensgen M, Wolf J F and Ibach H 1991 *Phys. Rev. Lett.* **67** 3543
[8] Pai W W, Ozcomert J S, Bartelt N C, Einstein T L and Reutt-Robey J E 1994 *Surf. Sci.* **307–309** 747
[9] Baumberger F, Hengsberger M, Muntwiler M, Shi M, Krempasky J, Patthey L, Osterwalder J and Greber T 2004 *Phys. Rev. Lett.* **92** 016803
[10] Knorr N, Brune H, Epple M, Hirstein A, Schneider M A and Kern K 2002 *Phys. Rev.* B **65** 115420
[11] Repp J, Moresco F, Meyer G, Rieder K H, Hyldgaard P and Persson M 2000 *Phys. Rev. Lett.* **85** 2981
[12] Lukas S, Witte G and Wöll C 2002 *Phys. Rev. Lett.* **88** 028301
[13] Shapiro A P, Miller T and Chiang T-C 1988 *Phys. Rev.* B **38** 1779
[14] Sánchez O, García J M, Segovia P, Alvarez J, Vázquez de Parga A L, Ortega J E, Prietsch M and Miranda R 1995 *Phys. Rev.* B **52** 7894
[15] Ortega J E, Speller S, Bachmann A R, Mascaraque A, Michel E G, Närmann A, Mugarza A, Rubio A and Himpsel F J 2000 *Phys. Rev. Lett.* **84** 6110
[16] Ortega J E, Mugarza A, Närmann A, Rubio A, Speller S, Bachmann A R, Lobo J, Michel E G and Himpsel F J 2001 *Surf. Sci.* **482–485** 764
[17] Mugarza A, Ortega J E, Mascaraque A, Michel E G, Altmann K N and Himpsel F J 2001 *Surf. Sci.* **482–485** 464
[18] Baumberger F, Greber T and Osterwalder J 2000 *Phys. Rev.* B **62** 15431
[19] Baumberger F, Greber T and Osterwalder J 2001 *Phys. Rev.* B **64** 195411
[20] Baumberger F, Greber T, Delley B and Osterwalder J 2002 *Phys. Rev. Lett.* **88** 237601
[21] Ortega J E, Mugarza A, Repain V, Rousset S, Pérez-Dieste V and Mascaraque A 2002 *Phys. Rev.* B **65** 165413
[22] Mugarza A, Mascaraque A, Repain V, Rousset S, Altmann K N, Himpsel F J, Koroteev Y M, Chulkov E V, García de Abajo F J and Ortega J E 2002 *Phys. Rev.* B **66** 245419

[23] Lobo J, Michel E G, Bachmann A R, Speller S, Roca L, Kuntze J and Ortega J E 2003 *J. Vac. Sci. Technol.* A **21** 1194
[24] Mugarza A, Ortega J E, Himpsel F J and García de Abajo F J 2003 *Phys. Rev.* B **67** 081404
[25] Mugarza A and Ortega J E 2003 *J. Phys.: Condens. Matter* **15** S3281
[26] Baumberger F, Hengsberger M, Muntwiler M, Shi M, Krempasky J, Patthey L, Osterwalder J and Greber T 2004 *Phys. Rev. Lett.* **92** 196805
[27] Ortega J E, Ruiz-Osés M, Cordón J, Mugarza A, Kuntze J and Schiller F 2005 *New J. Phys.* **7** 101
[28] Wang X Y, Shen X J, Osgood R M Jr, Haight R and Himpsel F J 1996 *Phys. Rev.* B **53** 15738
[29] Wang X Y, Shen X J and Osgood R M Jr 1997 *Phys. Rev.* B **56** 7665
[30] Shen X J, Kwak H, Mocuta D, Radojevic A M, Smadici S and Osgood R M Jr 2001 *Phys. Rev.* B **63** 165403
[31] Roth M, Pickel M, Jinxiong W, Weinelt M and Fauster T 2002 *Phys. Rev. Lett.* **88** 096802
[32] Smadici S, Mocuta D and Osgood R M 2004 *Phys. Rev.* B **69** 035415
[33] Smadici S and Osgood R M 2005 *Phys. Rev.* B **71** 165424
[34] Morgenstern K, Braun K F and Rieder K H 2002 *Phys. Rev. Lett.* **89** 226801
[35] Hansmann M, Pascual J I, Ceballos G, Rust H P and Horn K 2003 *Phys. Rev.* B **67** 121409(R)
[36] Bachmann A R 2002 Gestufte Cu-Oberflächen und Ag-Nano-Streifen: Atomare und Elektronische Struktur *PhD Thesis* Universität Osnabrück
[37] Rousset S, Repain V, Baudot G, Garreau Y and Lecoeur J 2003 *J. Phys.: Condens. Matter* **15** S3363
[38] Williams E D 1994 *Surf. Sci.* **299/300** 502
[39] Swamy K, Bertel E and Vilfan I 1999 *Surf. Sci.* **425** L369
[40] Schiller F, Ruiz-Osés M, Cordón J and Ortega J E 2005 *Phys. Rev. Lett.* **95** 066805
[41] de L Kronig R and Penney W G 1931 *Proc. R. Soc.* A **130** 499
[42] Davis L C, Everson M P, Jaklevic R C and Shen W 1991 *Phys. Rev.* B **43** 3821
[43] Borland R E 1961 *Proc. Phys. Soc. London* **78** 314
[44] Shiraki S, Fujisawa H, Nantoh M and Kawai M 2004 *Phys. Rev. Lett.* **92** 096102
[45] Avouris P and Lyo I-W 1994 *Science* **264** 942
[46] Bürgi L, Jeandupeux O, Hirstein A, Brune H and Kern K 1998 *Phys. Rev. Lett.* **81** 5370
[47] Eder R and Winter H 2004 *Phys. Rev.* B **70** 085413
[48] Lobo J, Michel E G, Bachmann A R, Speller S, Kuntze J and Ortega J E 2004 *Phys. Rev. Lett.* **93** 137602
[49] Louie S G, Thiry P, Pinchaux R, Pétroff Y, Chandesris D and Lecante J 1980 *Phys. Rev. Lett.* **44** 549
[50] Mugarza A, Ortega J E, Mascaraque A, Michel E G, Altmann K N and Himpsel F J 2000 *Phys. Rev.* B **62** 12672
[51] Bachmann A R, Ostendorf F and Speller S 2003 *J. Phys.: Condens. Matter* **15** S3337
[52] Bachmann A R, Mugarza A, Ortega J E and Speller S 2001 *Phys. Rev.* B **64** 153409
[53] Bachmann A R, Speller S, Mugarza A and Ortega J E 2003 *Surf. Sci.* **526** L143
[54] Ostendorf F 2002 Elektronische Zustände von Silber- und Kupfer-Nanostreifen *Master's Thesis* University of Osnabrück
[55] Ortega J E, Ruiz-Osés M and Kuntze J 2005 *Phys. Rev.* B **72** 195416